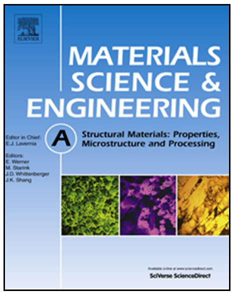

The influence of microstructure on the ductile to brittle transition and fracture behaviour of HVOF NiCoCrAlY coatings determined via small punch tensile testing

G.A. Jackson, W. Sun, D.G. McCartney

PII: S0921-5093(19)30421-6
DOI: https://doi.org/10.1016/j.msea.2019.03.108
Reference: MSA 37725

To appear in: *Materials Science & Engineering A*

Received Date: 26 November 2018
Revised Date: 24 March 2019
Accepted Date: 25 March 2019

Please cite this article as: G.A. Jackson, W. Sun, D.G. McCartney, The influence of microstructure on the ductile to brittle transition and fracture behaviour of HVOF NiCoCrAlY coatings determined via small punch tensile testing, *Materials Science & Engineering A* (2019), doi: https://doi.org/10.1016/j.msea.2019.03.108.

The Influence of Microstructure on the Ductile to Brittle Transition and Fracture Behaviour of HVOF NiCoCrAlY Coatings Determined Via Small Punch Tensile Testing

G.A.Jackson[1, a], W. Sun[1, b *], D.G. McCartney[1, c]

[1]Faculty of Engineering, University of Nottingham, University Park, Nottingham, NG7 2RD, UK

[a] George.Jackson3@nottingham.ac.uk, [b *] W.Sun@nottingham.ac.uk, [c]Graham.McCartney@nottingham.ac.uk

Keywords: Small Punch Tensile Testing, NiCoCrAlY, MCrAlY, HVOF, DBTT, Fracture, Mechanical properties.

Abstract.

The development of new thermal barrier coatings (TBC's) capable of increasing the efficiency of gas-powered turbines requires an understanding of how the tensile behavior and ductile to brittle transition temperature (DBTT) of MCrAlY bond coats are influenced by the coating microstructure. In this study, small punch tensile (SPT) tests were conducted on two high velocity oxy-fuel (HVOF) NiCoCrAlY coatings. Both coatings, referred to as BC1 and BC2, comprised a BCC β-NiAl matrix with FCC γ-Ni and TCP σ-Cr_2Co secondary phases. Coating BC2 also contained FCC γ'-Ni_3Al. Small punch tensile (SPT) tests were conducted on the coatings between RT and 750 °C. The DBTT's of coatings BC1 and BC2 were found to be 600-700 °C and 650-750 °C respectively. Lower phase fractions of γ-Ni were shown to increase the DBTT. The main mode of crack propagation in both coatings was intergranular fracture along the grain boundaries of differing phases. Schematic models were used to demonstrate the change in tensile behavior across the DBTT and explain the influence of the coating microstructure on the fracture behavior of both coatings.

1. Introduction

Thermal barrier coatings (TBC's) are multilayer composite systems comprising: a ceramic top coat, a metallic alloy bond coat and substrate alloy. TBC's are extensively employed in gas turbines to lower the operating temperature of alloy substrate; typically a nickel-based superalloy [1-3]. The ceramic top coat provides thermal resistance to the system and is adhered to the substrate through the bond coat, which provides oxidation resistance to the substrate and accommodates strain mismatch between the substrate and ceramic top coat. Recently, MCrAlY (M=Ni,Co) overlay bond coats deposited by high velocity oxy-fuel (HVOF) thermal spraying have become widely used in TBC's because of advantages such as low cost and the possibility to employ complex MCrAlY alloys with tailored microstructures [4-6]. The composition of HVOF MCrAlY bond coats can be adjusted without needing to alter the composition of the substrate; offering greater flexibility over traditional diffusion coatings which require a coating composition similar to the substrate composition [1, 7-8]. MCrAlY's can comprise FCC γ-Ni, BCC B2-β-NiAl, ordered γ'-Ni_3(Al,Ti) and σ-(Cr,Co) [9-11]. The B2-β-NiAl phase, commonly present in MCrAlY overlay coatings, is brittle at lower temperatures and shows increasing strain to fracture above a critical temperature termed the ductile to brittle transition temperature (DBTT); around 750 °C for NiAl. Hence, overlay coatings containing β-NiAl also exhibit a transition in strain to cracking behaviour above the DBTT [12-13]. This can be problematic for TBC's that undergo thermal cycling as cracks can form as the operating temperature decreases below the DBTT. Hence, detailed understanding of the DBTT and temperature dependent mechanical behaviour is essential in order to develop life prediction models of TBC's.

Moreover, as the microstructure of a bond coat is directly influenced by the thermal spray deposition process and any subsequent thermal treatment during manufacturing [4, 6, 14], it is essential to determine bond coat mechanical properties of thin, freestanding coatings manufactured in a similar way to industrial TBC processes.

Investigations into the mechanical properties of MCrAlY coatings have been carried out using a variety of experimental techniques (i.e. 4 point bending, local indentation) [5, 14-18] but there is still little consistent data for any single MCrAlY coating. Recently, studies have employed the small punch tensile (SPT) test to determine the mechanical properties and DBTT of MCrAlY coatings [12, 19-20]. The SPT test is suitable for coatings as it employs small specimens: 8 mm diameter discs of 0.5 mm thickness. The SPT test has been widely validated as an effective method to determine the mechanical properties and DBTT of steels [21-27] and the recent studies have demonstrated the applicability of the SPT test for MCrAlY coatings.

The current work aims to investigate the influence of coating microstructure on the mechanical properties and ductile to brittle transition behaviour of two NiCoCrAlY bond coats manufactured by HVOF thermally spraying, which have potential as new bond coat alloys. The DBTT and mechanical properties of the coatings were determined by small punch tensile testing between RT and 750 °C. The macroscopic and microscopic fracture behaviour of both coatings was investigated with reference to the coating microstructures.

2. Experimental Methods

2.1. Materials, HVOF Thermal Spraying and Heat Treatment.

The coatings were prepared by HVOF thermal spraying using powders with the following nominal composition: Ni-20Co-22.3Cr-12.2Al-0.3Y and Ni-20Co-22.3Cr-12.2Al-0.3Y-4Ta (wt.%) denoted BC1 and BC2 respectively. The coatings were deposited onto mild steel substrates of dimensions 60 × 25 × 1.8 mm using a Met Jet III liquid fuel HVOF gun. The spraying procedure is detailed elsewhere [28]. The mild steel substrates were not grit blasted to aid debonding after spraying. Coatings were sprayed to a thickness of approximately 600 µm and were then debonded from the mild steel by bending around a mandrel to produce free standing coatings. Vacuum heat treatment was carried out on free-standing samples at 1100 °C for two hours in an Elite Thermal Systems TVH12 vacuum tube furnace held at approximately 10^{-9} bar followed by furnace cooling to room temperature over a period of 6 hours. This treatment was applied in order to approximately replicate the initial heat treatment given to bond coats during the manufacture of thermal barrier coatings. This type of heat treatment has been shown to reduce the porosity commonly present within sprayed coatings and allow the precipitation of secondary phases [19, 20, 28]. Specimens for SPT tests, in the form of 8 mm diameter discs, were cut from the heat treated coatings by electro-discharge machining. The specimens were ground down from the as-deposited thickness to a final thickness of 400 µm on 1200 grade silicon carbide paper. The final thickness, taken as the average of four measurements per specimen, was controlled to within ± 5 µm as measured by a digital micrometre and both surfaces had the same finely ground surface finish.

2.2 Microstructural Characterisation.

Cross sections of the heat treated coatings were mounted, ground and polished to a 1 µm diamond finish. Scanning electron microscopy (SEM) was carried out using a FEI XL30 scanning electron microscope equipped with an Oxford Instrument Link ISIS-3000 energy dispersive X-ray analysis (EDX) detector. Backscattered electrons (BSE) were used to form images and semi-quantitative EDX was utilised to aid phase identification through chemical microanalysis. Samples for electron back-scatter diffraction (EBSD) required a further stage of chemical/mechanical polishing using colloidal silica to achieve a surface finish of 0.02 µm with minimal surface deformation. SEM-based EBSD was carried out on a Zeiss 1530 VP field emission gun scanning electron microscope

(Carl Zeiss, Inc., Maple Grove, MN) with an EDAX Pegasus combined electron backscatter diffraction system (EDAX, Mahwah, NJ, USA). The EBSD patterns were recorded at a specimen tilt angle of 70 ° with an accelerating voltage of 20 kV and a beam current of 26 nA. EBSD maps of the specimen were collected over an area of 50 µm × 50 µm at a step size of 0.1 µm.

BSE images and EBSD phase distribution maps were used to measure the volume fractions of the different phases within the coating. Quantitative image analysis was carried out using the ImageJ and Gimp 2.0 software packages. Volume fractions are the mean of four measurements.

2.3 Small Punch Tensile Testing.

Displacement controlled small punch tests were carried out at a displacement rate of 1×10^{-6} ms^{-1} at room temperature (RT) and between 500-750 °C on a custom built rig installed on a Tinius Olsen H5KS single column materials testing machine. The temperature range was chosen to achieve brittle failure at the lower temperature and ductile failure at the higher temperature. A schematic of the small punch rig is shown in Figure 1. Full details on the SPC rig can be found at [20]. A three tier, 3 kW furnace was used to heat the specimens. Three K-type thermocouples, accurate to 5 °C, were used to measure the furnace temperature in the top, middle and bottom tiers. The temperature variation across the three tiers was ≤ 2 °C. Temperature variations across the specimen were considered to be negligible due to the small specimen size and minimal temperature variation across the furnace. All tests were carried out in accordance with the CEN workshop agreement [29] in a temperature controlled room held at 21 °C. The load was applied through a 2.5 kN load cell and the punch head displacement was measured by two linear variable differential transformers (LVDTs).

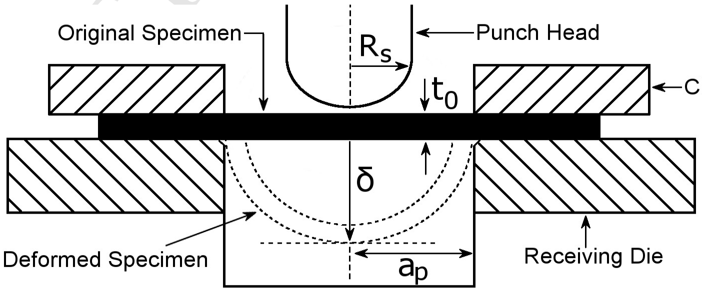

Figure 1. Schematic (not drawn to scale) cross section of the small punch rig showing the application of load through a hemispherical punch head and resultant specimen displacement (δ) where a_p, R_s and t_0 are the radius of the receiving hole (4 mm), punch head radius (1 mm) and specimen thickness (0.4 mm) respectively.

3. Data Analysis

Small punch tensile testing induces a complex biaxial stress state in test specimens [21, 30-32]. The load-displacement curves obtained from SPT tests typically exhibit up to four distinct bending regions [33], as shown in Figure 2, and there is currently no analytical solution available that allows strain to be calculated from all four bending regions without finite element analysis. The available solutions allow elastic biaxial strain to be calculated within the elastic bending regime of a SPT curve [21] and biaxial fracture strain to be calculated at the point of fracture [30]. However, there are also multiple approaches to determine the point of failure in a SPT test. As such, the methodology used to calculate strain from SPT tests must be carefully considered in order to allow accurate interpretation of the calculated values. The following section illustrates the equations used in this work to calculate strain and the method used to identify the point of failure in the SPT load-displacement curves.

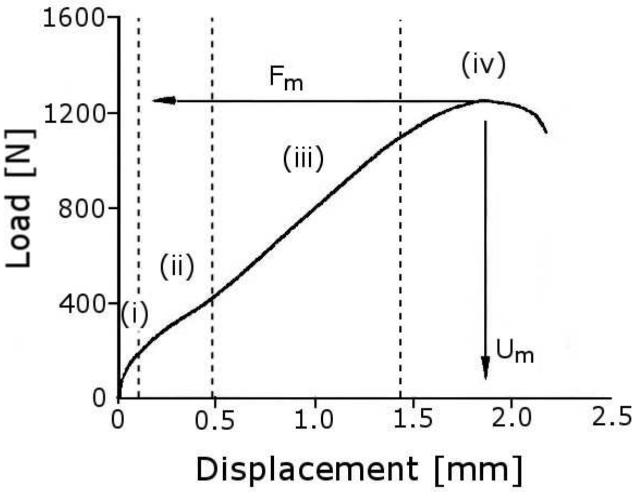

Figure 2. Schematic diagram of a typical load-displacement curve obtained from small punch tensile testing of a ductile material [33]. The four bending regions are: (i) elastic bending; (ii) plastic bending; (iii) membrane stretching and (iv) progressive plastic instability. F_m and U_m indicate the maximum load and the displacement at maximum load respectively.

3.1 Determination of strain from SPT test

In small punch tensile (SPT) tests the elastic biaxial strain in the specimen is calculated by considering biaxial bending of a thin disc clamped at its circumference. A solution to calculate the elastic biaxial strain (ε) at the outer surface of the sample at its central point was provided by Huang et al. [21]:

$$\varepsilon = \frac{t_0\,\delta}{({a_p}^2 + \delta^2)}\,. \tag{1}$$

where t_0 is the original specimen thickness (mm), δ is the specimen displacement (mm) and a_p is the radius of the receiving hole (mm), as shown in Figure 1.

The solution provided by Huang et al. [21] allows the elastic biaxial strain to be calculated within the elastic bending regime of the SPT load-displacement curve but ceases to be applicable once plastic deformation occurs. The elastic-plastic biaxial stain cannot be related to the punch displacement by simple analytical equations due to the complex nature of the SPT load-displacement curve, although finite element solutions are available for specific alloys and test configurations. However, a semi-empirical solution can be used to calculate the equivalent biaxial strain of a SPT specimen once it has fractured. The semi-empirical relationship was provided by Mao et al. [30] and calculates the biaxial fracture strain (ε^*) of a small punch sample from the displacement at fracture (δ^*) and original specimen thickness (t_0). The solution was derived by correlating the thickness change at fracture of various alloys to the specimen displacement and rig geometry. The solution can be used to calculate the approximate biaxial strain at fracture for SPT specimens exhibiting plastic deformation.

$$\varepsilon^* = 0.15\left(\frac{\delta^*}{t_0}\right)^{1.5} \tag{2}$$

3.2 Identification of point of fracture

The DBTT of coatings is commonly identified by plotting coating ductility as a function of temperature and identifying the transition from high temperature ductile behaviour to low temperature brittle behaviour [1]. A schematic demonstrating this is shown in Figure 3, where the DBTT is defined as the difference between the highest temperature at which no ductile behaviour is observed, and the lowest temperature at which full ductile behaviour is observed. The ductility is measured as the strain to initiate first cracking as is typical for bond coats [34].

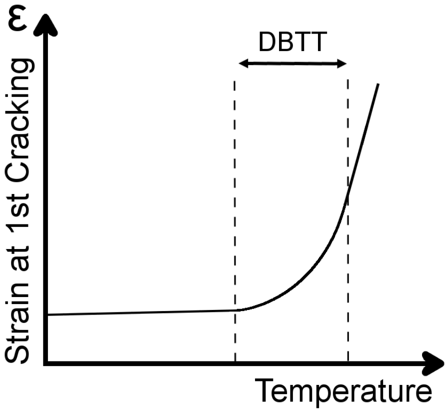

Figure 3. Schematic showing ductility, measured as strain to first cracking, as a function of temperature. The DBTT is measured as the transition from high temperature ductile behaviour to low temperature

brittle behaviour. Schematic based on figures in [1].

A crucial element of the SPT test is the ability to assess, in a reproducible manner, this strain to initiate first cracking from the experimental SPT test curve. For ductile materials the point of failure in a SP tensile test is often taken at the maximum load [29]. However, brittle materials may exhibit load drops prior to the maximum load, which are known to be associated with cracking in the sample [31]. Materials may also exhibit a characteristic change in slope of the load-displacement curve. Such changes may occur due to cracks forming on the tensile surface of the specimen. The deflection of the disc varies as the cube of the thickness, hence the load-displacement curve will be strongly altered when the outside fibres of the disc first crack [21].

Therefore in the present study the point of failure onset is defined as the first measurable load-drop or a characteristic change in the slope of the load-displacement curve which is not associated with one of the four bending regions typically associated with SPT testing i.e. elastic bending (i), plastic bending (ii), membrane stretching (iii) and maximum load and progressive plastic instability (iv) [33].

4. Results

4.1 Microstructure of Heat Treated Coatings.

Figure 4 and Figure 5 show BSE images and EBSD maps of coatings BC1 and BC2 respectively. The BSE images show both coatings exhibit thin, dark elongated features which are regions of Al_2O_3 that formed during spraying. The oxide content was measured as ~ 4 vol.% for both coatings.

In the BSE images of both coatings the dark grey phase corresponds to the BCC β-NiAl phase as identified by EDX. The light grey phase is either FCC γ-Ni or TCP σ-Cr_2Co phase, both of which exhibit a similar BSE contrast. The sigma phase is referred to as σ-Cr_2Co as this reflects the phase composition more accurately than σ-CrCo. This observation has previously been reported by Toscano et al. [10]. In the case of the BC2 coating, the bright phase in the BSE images corresponds to the FCC γ'-Ni_3Al phase. In the EBSD phase maps the β-NiAl and σ-Cr_2Co phases can be identified and are coloured red and yellow respectively. The γ-Ni and γ'-Ni_3Al phases are both FCC so could not be distinguished in the phase maps. As such, both phases are coloured green. The phase fractions for each coating were calculated using a combination of the BSE images, in which regions of γ'-Ni_3Al could be distinguished, and the EBSD phase maps, in which regions of σ-Cr_2Co could be distinguished. The phase fraction of γ-Ni was then calculated from the difference between the BSE images and EBSD phase maps. The phase fractions for each coating as listed in Table 1 and the composition of each phase, as measured by EDX, is presented in Table 2.

The random assortment of colours in the IPF (Z) maps indicates that there is no preferred grain orientation for either coating. The finer grains indicate areas of the coatings which underwent melting and resolidification during thermal spraying. The areas of larger grains highlight powder particles which retained in part, the original powder microstructure during HVOF thermal spraying.

	Phase Fraction (vol.%)			
	β-NiAl	γ-Ni	σ-Cr_2Co	γ'-Ni_3Al
BC1	60 ± 2	27 ± 2	13 ± 2	-
BC2	56 ± 2	14 ± 2	21 ± 2	9 ± 1

Table 1. Phase fractions (vol.%) of coatings BC1 and BC2 as measured by image analysis using a combination of BSE images and EBSD phase maps.

Coating	Phase	**Phase Composition (wt.%)**				
		Ni	Co	Cr	Al	Ta
BC1	β-NiAl	57 ± 3	14 ± 3	8 ± 1	20 ± 2	-
	γ-Ni	38 ± 2	29 ± 3	27 ± 2	8 ± 1	-
	σ-Cr_2Co	19 ± 2	27 ± 2	49 ± 2	3 ± 1	-
BC2	β-NiAl	52 ± 2	17 ± 1	9 ± 1	20 ± 1	2 ± 1
	γ-Ni	36 ± 4	23 ± 1	27 ± 4	10 ± 2	3 ± 1
	σ-Cr_2Co	18 ± 2	27 ± 1	47 ± 2	3 ± 1	4 ± 1
	γ'-Ni_3Al	48 ± 2	15 ± 1	8 ± 1	10 ± 1	18 ± 1

Table 2. Phase compositions of coatings BC1 and BC2 as measured by EDX analysis. The values shown are an average of 4 spectra and the errors shown are the standard deviations.

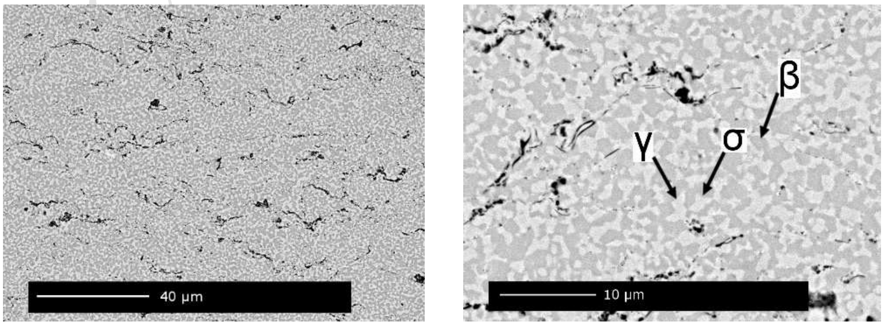

(a) (b)

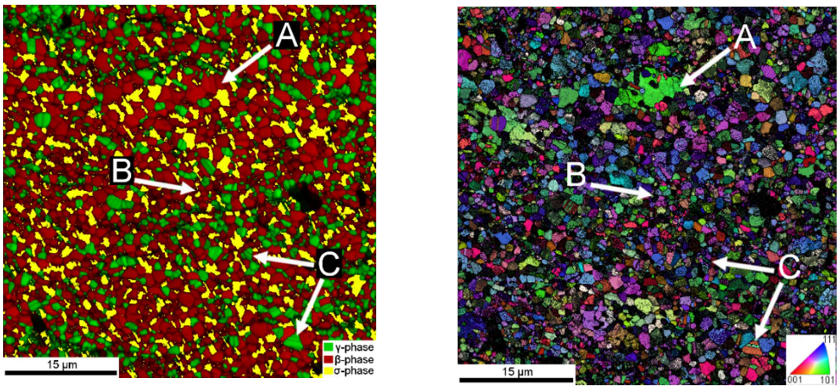

(c) (d)

Figure 4. BSE images (a-b) of the heat treated BC1 coating. The light contrast phase is an FCC Ni-γ-phase and the dark contrast phase is a BCC NiAl-β-phase. The dark regions are Al_2O_3 oxides. Images (c) and (d) are EBSD scans presented as a phase map and grain orientation map respectively. The letters A and B indicate areas of large and fine grains respectively. The letter C indicates twinning in the γ-Ni phase.

4.2 Load–Displacement Curves and Macroscopic Fracture Patterns

Representative load-displacement plots are shown in Figure 6 for BC1 and BC2 specimens following SPT tests at room temperature (RT) and between 500-750 °C. The corresponding macroscopic fracture patterns observed on the tensile surfaces of the specimens are shown in Figure 7 and Figure 8 for coatings BC1 and BC2 respectively.

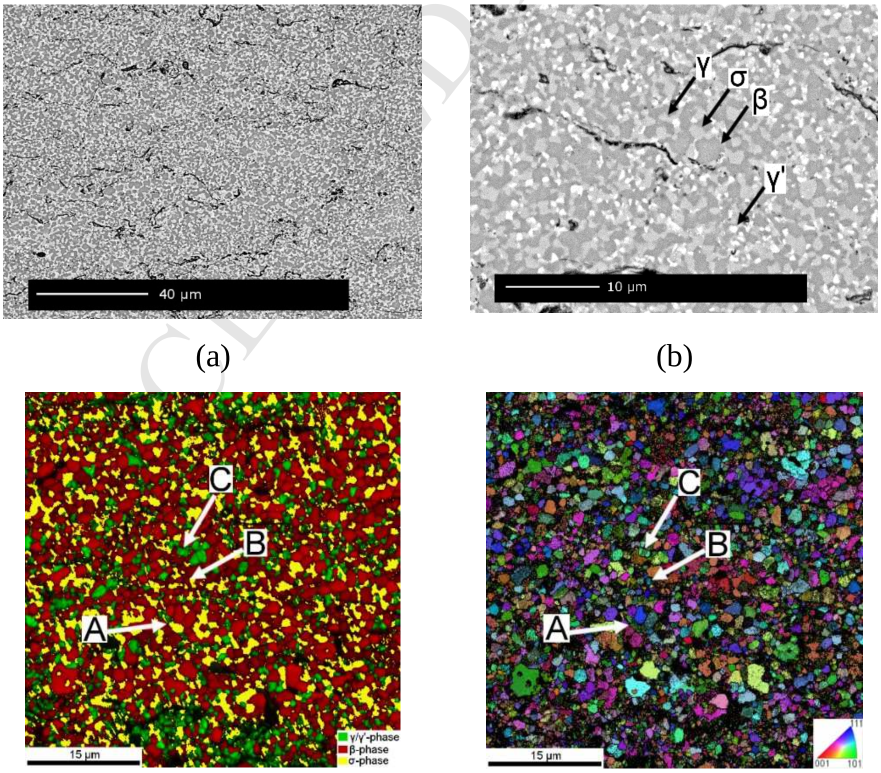

(a) (b)

(c) (d)

Figure 5. BSE images (a-b) of the heat treated BC2 coating. The light contrast phase is a FCC Ni-γ-phase and the dark contrast phase is a BCC NiAl-β-phase. The dark regions are Al_2O_3 oxides. Images (c) and (d)

are EBSD scans presented as a phase map and grain orientation map respectively. The letters A and B indicate areas of large and fine grains respectively. The letter C indicates twinning in the γ-Ni phase.

There is a distinct change in the load-displacement behaviour for both coatings as the temperature is increased. At high temperatures (700 and 750 °C), the curves are similar to those reported elsewhere for ductile materials [22-23, 35] and display an initial linear region of elastic behaviour followed by plastic deformation, membrane stretching, maximum load and then progressive plastic instability, as indicated in regions (i)-(iv) in Figure 2 respectively. Failure occurs shortly after the maximum load, as has been observed for steels. At the lower temperatures, down from 600 and 650 °C for coatings BC1 and BC2 respectively, the curves are predominately linear and feature sharp load drops which have been shown to indicate failure in non-ductile materials [20, 31, 36]. Hence, the point of failure, indicated by the arrows in Figure 6, is taken at the first load drop or characteristic change in the slope of the curve that is not associated with one of the four bending regions described above.

The macroscopic fracture patterns shown in Figure 7 and Figure 8 clearly indicate the change in load-displacement behaviour corresponds to a change in macroscopic fracture behaviour for both coatings. At RT, cracks formed at the centre of the tensile surfaces of both coatings and propagated radially. As the punch head continued to push through the specimens the cracks propagated further and eventually caused the centre of the specimens to split into fragments, as shown in Figure 8c for the BC2 specimen tested at 500 °C. This type of cracking also occurred for the BC1 specimen tested at 500 °C but the central fragments became completely detached. This type of fracture has been previously reported for SPT specimens and is known to be associated with brittle failure [36].

At 700 and 750 °C for coatings BC1 and BC2 respectively, the coatings exhibited ductile behaviour and specimen failure occurred through the growth of a circumferential crack, shown clearly in Figure 7d and Figure 8d for the BC1 and BC2 coatings respectively. The cracks developed at a radial offset from the centre of the specimen and propagated along a circumferential path. This type of circumferential cracking is caused by thinning of the sample due to membrane stretching and is known to be associated with ductile failure during SPT testing [37].

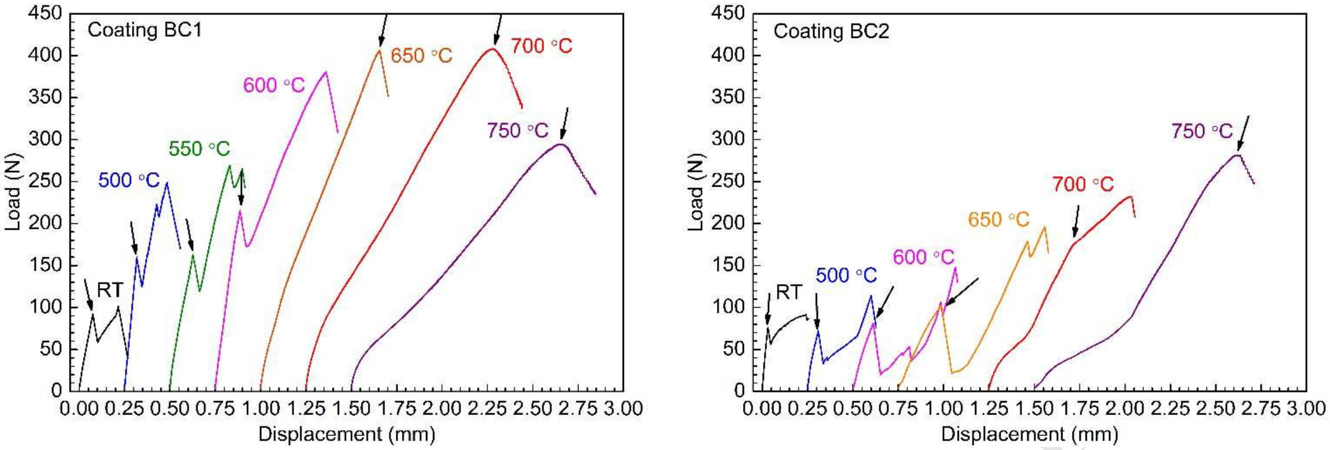

(a) (b)

Figure 6. Representative load-displacement curves for small punch tensile tests carried out between room temperature and 750 °C for coatings BC1 (a) and BC2 (b). The BC1 coating exhibits brittle behaviour down from 600 °C and ductile behaviour above 700 °C whereas coating BC2 exhibits brittle behaviour down from 650 °C and ductile behaviour above 750 °C. The arrows indicate the point of failure.

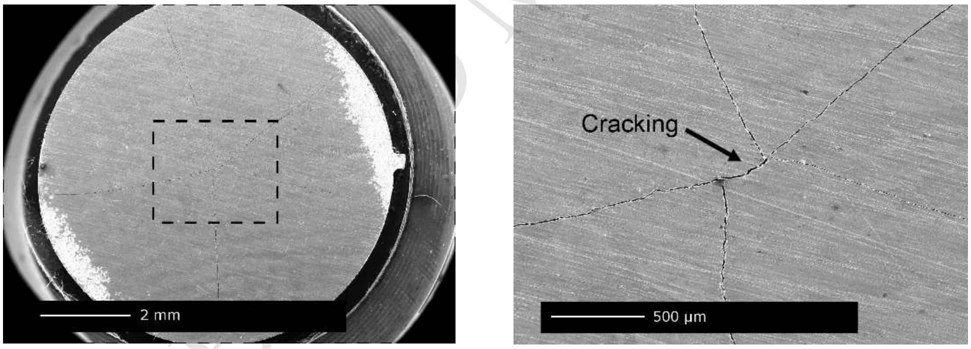

(a) RT (b) RT

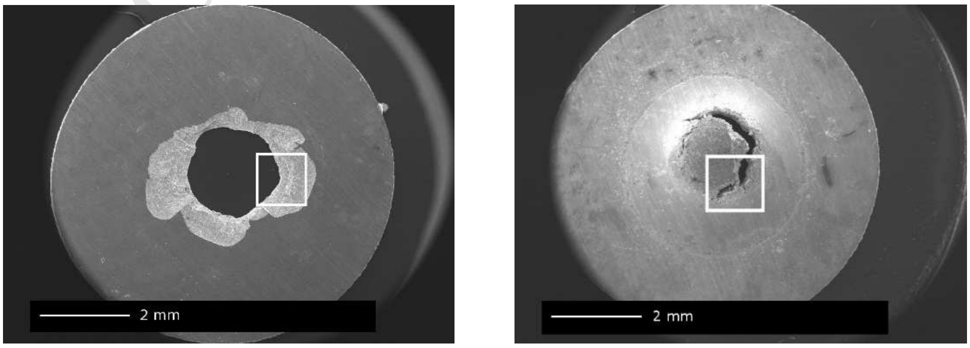

(c) 500 °C (d) 700 °C

Figure 7. Tensile surfaces of the BC1 coating following SPT testing at (a-b) RT, (c) 500 °C and (d) 700 °C. The white boxes in (c) and (d) indicate the areas shown at higher magnification in Figure 10 and Figure 12 respectively.

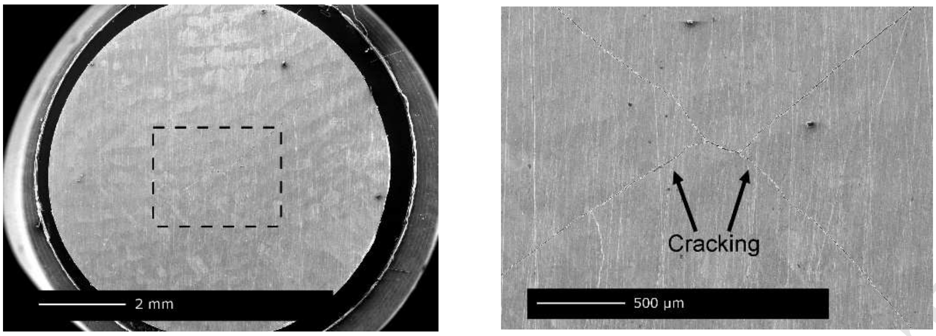

(a) RT (b) RT

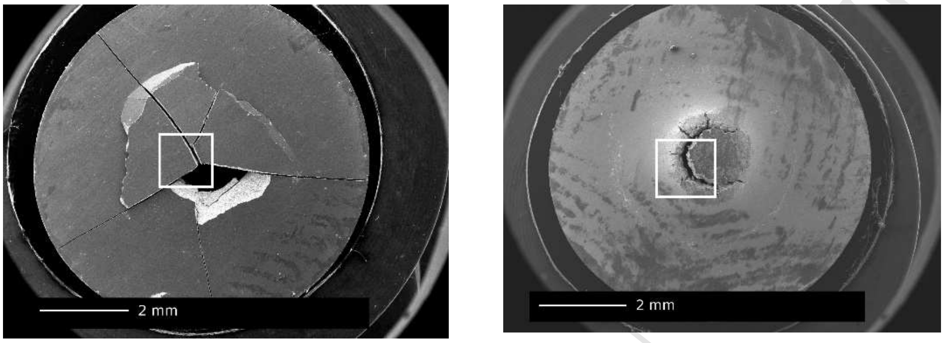

(c) 500 °C (d) 750 °C

Figure 8. Tensile surfaces of the BC2 coating following SPT testing at (a-b) RT, (c) 500 °C and (d) 750 °C. The white boxes in (c) and (d) indicate the areas shown at higher magnification in Figure 11 and Figure 13 respectively.

4.3 Ductile to Brittle Transition Temperature

The strain to first cracking as a function of temperature is shown for both coatings in Figure 9. For coating BC1, there is only a small increase in the strain at first cracking between RT and 600 °C, indicating that the ductility of the BC1 coating does not change significantly over that temperature range. Between 600 and 700 °C there is a large increase in the strain at first cracking which demonstrates there is a significant change in the ductility of the coating. Similar behavior is observed for coating BC2 with the increase in strain to cracking occurring between 650-750 °C. Therefore, the DBTT of coatings BC1 and BC2 are established as 600-700 °C and 650-750 °C respectively based on the definition of DBTT as explained in Figure 3.

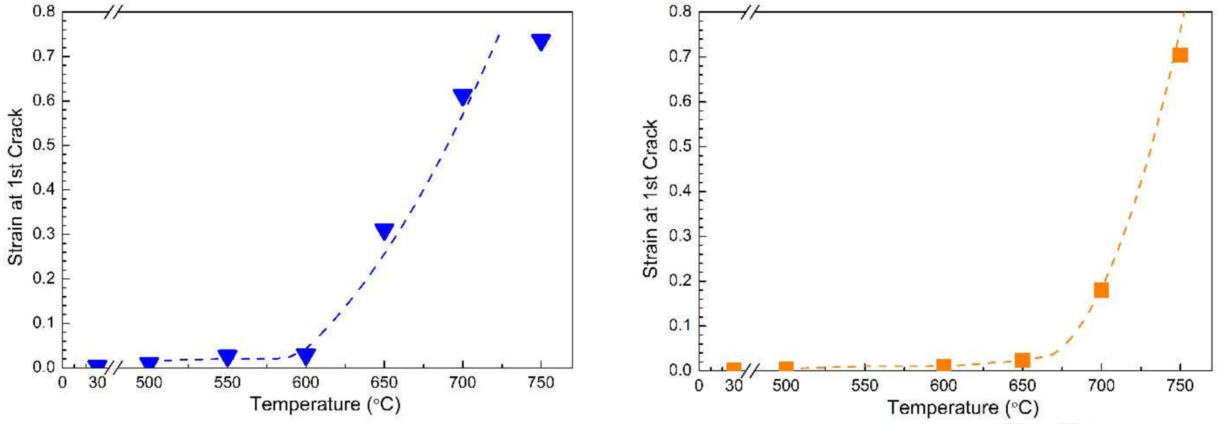

(a) (b)

Figure 9. The strain to first cracking as a function of temperature for coatings (a) BC1 and (b) BC2.

4.4 Microscopic Fracture Path Analysis

4.4.1 Low Temperature Fracture

The change in fracture behaviour exhibited by both coatings across the DBTT can be better understood by looking at the microscopic fracture behaviour of each coating above and below the DBTT. Plan view images of the BC1 and BC2 coatings following SPT testing at 500 °C, taken from the areas indicated by the white boxes in Figures 7c and 8c respectively, are shown in Figure 10 and Figure 11 respectively, where (a) is a BSE image, (b) is an EBSD phase map and (c) is an inverse pole figure (IPF) (Z) that assigns a colour to separate grains based on orientation. The letter A indicates evidence of transgranular fracture through the β-NiAl phase, evidenced by a similar orientation of the β-NiAl phase grains either side of crack path. The letter B indicates evidence of intergranular fracture along the phase boundaries between the matrix β-NiAl phase and the secondary γ-Ni and σ-Cr_2Co phases. This is the dominant mode of fracture in the BC1 coating at 500 °C. The letter C indicates evidence of transgranular fracture through a grain of σ-Cr_2Co phase. Transgranular fracture through the β-NiAl and σ-Cr_2Co-phases appears to occur when the phase boundary is at a large angle to the direction of crack growth. There is no evidence of transgranular fracture through a grain of γ-Ni phase. It can be concluded that intergranular fracture along phase boundaries is the dominant mode of fracture in the BC1 coating at 500 °C and transgranular fracture through the β-NiAl and σ-Cr_2Co phases is a secondary mode of fracture.

Figure 11 shows two well defined cracks in the BC2 specimen following SPT testing at 500 °C. The letter A indicates evidence of transgranular fracture through a grain of β-NiAl phase. The letters B and C indicate evidence of intergranular fracture along the β-NiAl/σ-Cr_2Co and β-NiAl/γ’-Ni_3Al phase boundaries respectively. The letter D indicates evidence of transgranular fracture through a grain of σ-Cr_2Co phase. There is no evidence of intergranular fracture between two grains of β-NiAl phase. The preferential path for crack propagation in the BC2 coating at 500 °C is variable: one mode of fracture is transgranular fracture through the β-NiAl phase; there is clear evidence of a crack originating within a grain of β-NiAl phase, indicated by A in Figure 11. Another mode of fracture is intergranular fracture along phase boundaries which is the dominant mode of fracture where phase boundaries between differing phases exist. The third mode of propagation is transgranular fracture through the σ-Cr_2Co phase. This type of fracture appears to occur when the phase boundary is at a large angle to the direction of the crack growth. There is no evidence of transgranular through the γ-Ni or γ'-Ni_3Al phase in the BC2 coating at 500 °C.

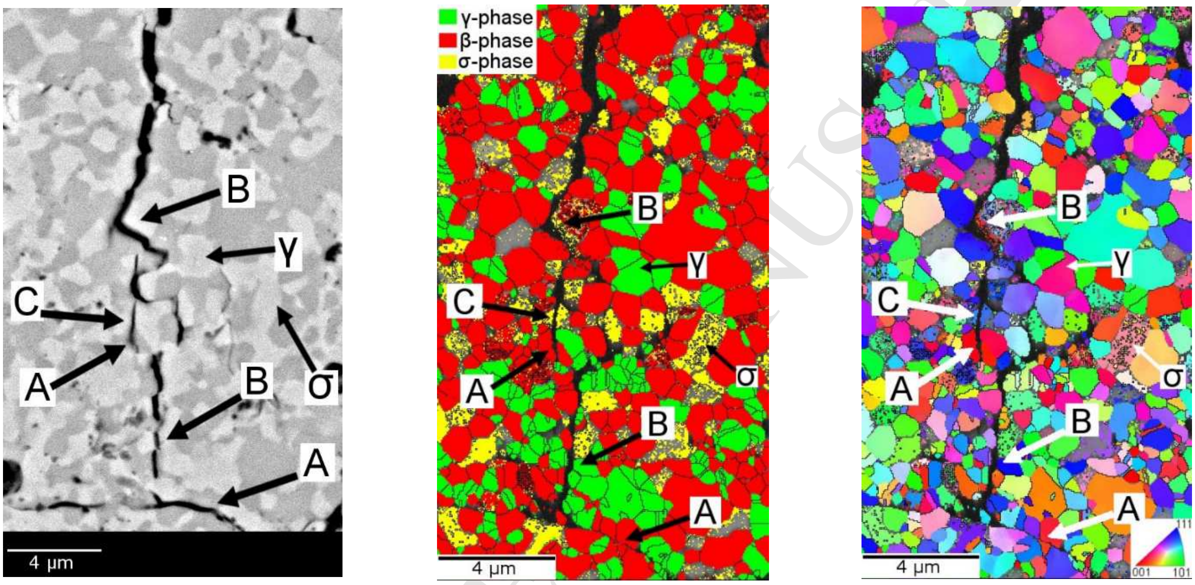

(a) (b) (c)

Figure 10. BSE image (a) and EBSD phase map (b) and IPF (Z) map (c) of a cross section of coating BC1 following SPT testing at 500 °C. The letter A indicates evidence of transgranular fracture through the β-NiAl phase, the letter B indicates evidence of intergranular fracture along the phase boundaries between the β-NiAl matrix phase and secondary γ-Ni and σ-Cr_2Co phases. The letter C indicates evidence of transgranular fracture through a grain of σ-Cr_2Co phase.

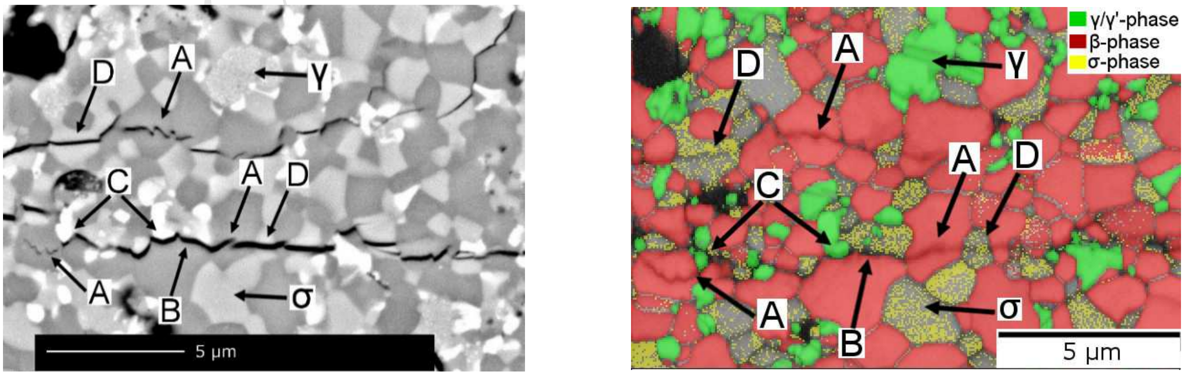

(a) (b)

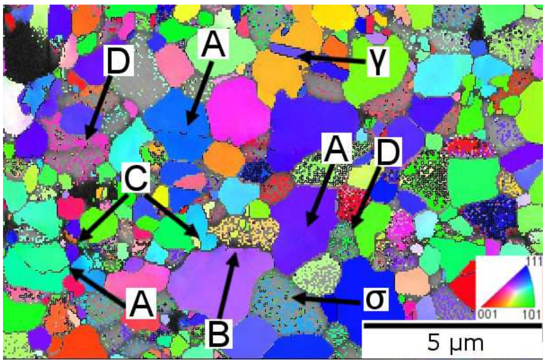

(c)

Figure 11. BSE image (a) and EBSD phase map (b) and IPF (Z) map (c) of a cross section of coating BC2 following SPT testing at 500 °C. The letter A indicates evidence of transgranular fracture through the β-NiAl phase, the letter B indicates evidence of intergranular fracture along the phase boundaries between the β-NiAl matrix phase and secondary γ-Ni and σ-Cr_2Co phases. The letter C indicates evidence of transgranular fracture through a grain of σ-Cr_2Co phase.

4.4.2 High temperature fracture

Figure 12 and Figure 13 show cross sections of the BC1 and BC2 coatings tested at 700 and 750 °C respectively where (a) is a BSE image, (b) is an EBSD phase map and (c) is an inverse pole figure (IPF) (Z). The areas shown are highlighted by the white boxes in Figures 7d and 8d for the BC1 and BC2 coatings respectively. Considering coating BC1 first, the crack shown in Figure 12a is significantly wider than the low temperature cracks shown in Figure 10. This indicates slow crack growth and ductile tearing; clearly different to the thin cracks observed at 500 °C. It is clear from Figure 12a that the crack tip is growing in between regions of the dark contrast NiAl-β phase and the light contrast γ-Ni/σ-Cr_2Co phase.

Figure 12b is a BSE image showing an example of void formation in the BC1 coating in the area of high tensile stress in a SPT specimen. The letter A indicates evidence of void formation at the phase boundaries between the β-NiAl phase, the γ-Ni phase and/or the σ-Cr_2Co phase. This intergranular void formation at the phase boundaries is the predominant type of void formation in the BC1 coating at 700 °C and explains the phase boundary crack growth observed in Figure 12a.

Figure 13 shows an example of void formation and crack growth in the BC2 coating at 750 °C. The letter A indicates evidence of void formation at the phase boundaries between the β-NiAl phase, the γ-Ni/γ'-Ni_3Al phase and/or the σ-Cr_2Co phase. The letter B indicates evidence of intergranular fracture along the grain boundaries of adjacent grains of β-NiAl phase. The letter C indicates evidence of intergranular crack growth along the phase boundaries between the β-NiAl phase and/or the γ-Ni, γ'-Ni_3Al and σ-Cr_2Co phases. The intergranular crack growth along grain boundaries of differing phases appears to be the dominant mode of crack growth in the BC2 coating at 750 °C and is most likely caused by the void formation at the phase boundaries indicated by A. Intergranular crack growth between adjacent grains of β-NiAl phase appears to be a secondary mode of fracture.

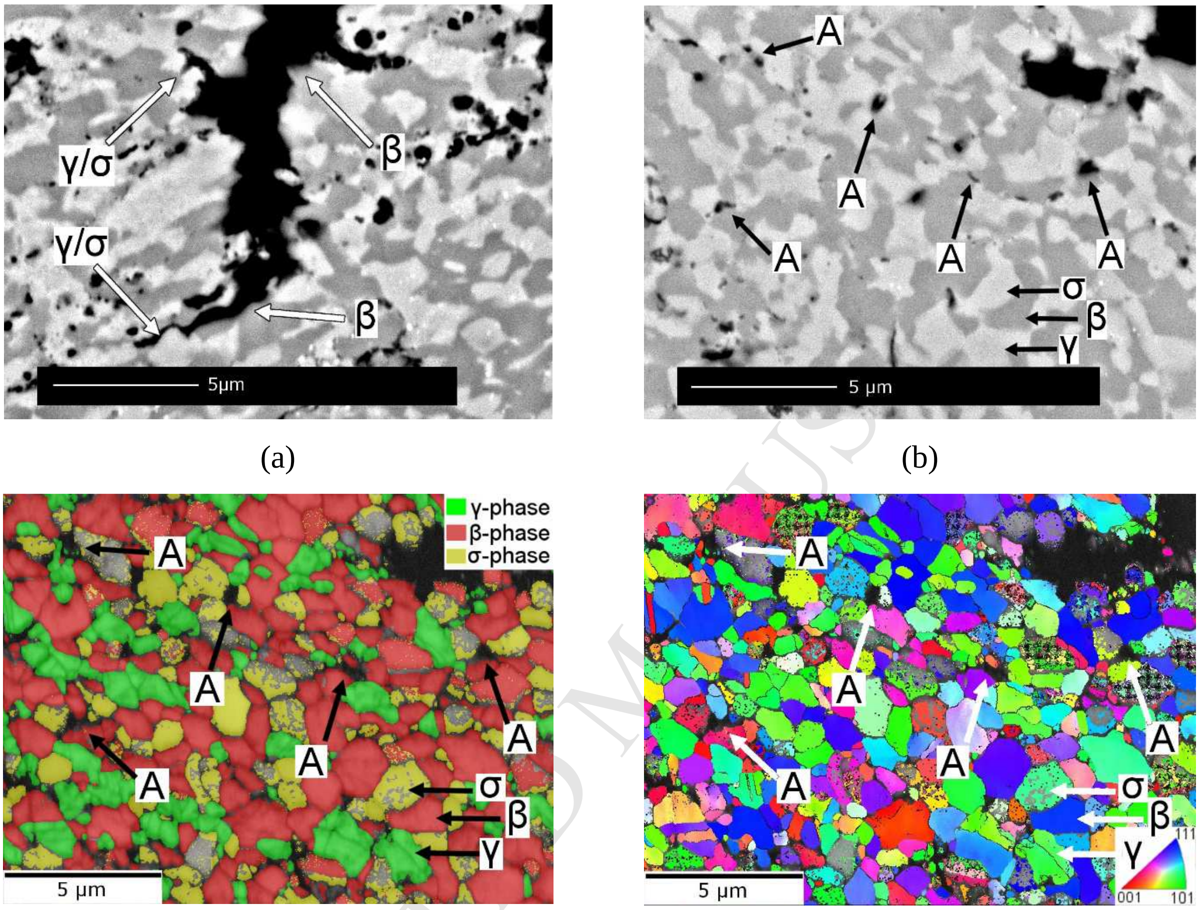

(a) (b)

(c) (d)

Figure 12. BSE images (a-b), EBSD phase map (c) and IPFZ map (d) of coating BC1 following SPT testing at 700 °C. The letter A indicates evidence of void formation at the phase boundaries between the β-NiAl phase, the γ-Ni phase and/or the σ-Cr_2Co phase.

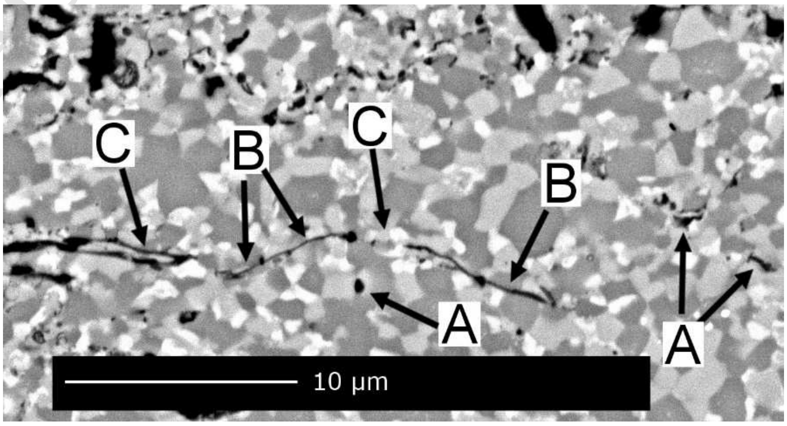

(a)

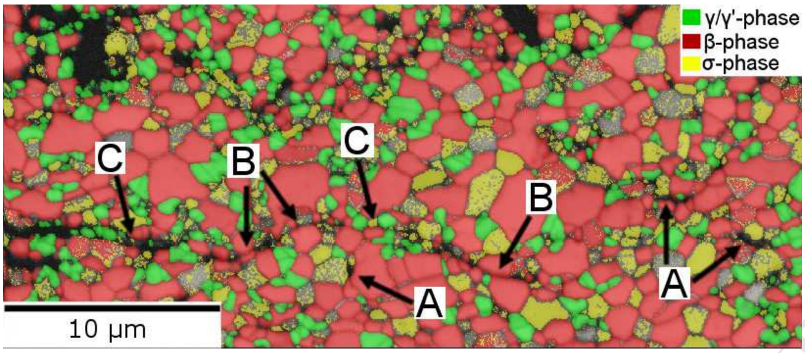

(b)

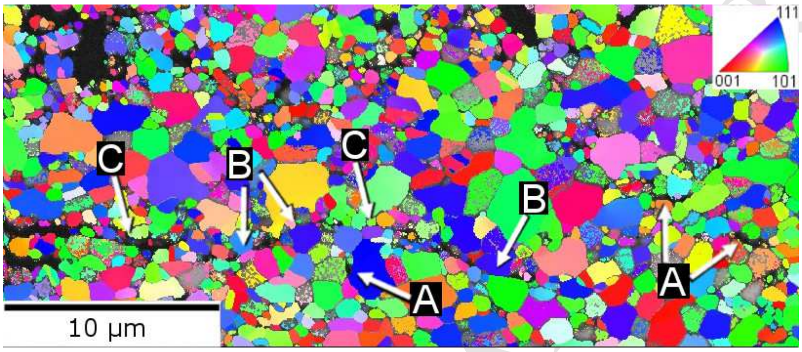

(c)

Figure 13. BSE image (a) and EBSD phase map (b) and IPFZ map (c) of a cross section of coating BC2 following SPT testing at 750 °C. The letter A indicates evidence of void formation at the phase boundaries between the β-NiAl phase, the γ-Ni/γ'-Ni_3Al phase and/or the σ-Cr_2Co phase. The letter B indicates evidence of intergranular fracture along the grain boundaries of adjacent grains of β-NiAl phase. The letter C indicates evidence of intergranular crack growth along the phase boundaries between the β-NiAl phase and/or the γ-Ni, γ'-Ni_3Al and σ-Cr_2Co phases.

5. Discussion

5.1 Influence of Microstructure on Ductile to Brittle Transition Temperature

The only available study concerning the DBTT of MCrAlY alloys with compositions similar to the BC1 and BC2 alloys was conducted by Hesbur and Miner [38], who reported a Ni-20Co-17Cr-14Al-0.5Y coating exhibited a marked increase in ductility above 500 °C; which is consistent with the current findings. The DBTT is known to be sensitive to a number of factors including composition, phase distribution, microstructure and manufacturing process [1, 34]. As the BC1 and BC2 coatings received the same manufacturing process, the difference in the DBTT's can be discussed with respect to the coating compositions and microstructures. In general, the β-NiAl phase is considered the phase responsible for the ductile to brittle transition in MCrAlY alloys; increasing the phase fraction of β-NiAl is considered to increase the DBTT [1, 34-35, 39].This relationship is not useful for comparing the DBTT's of the BC1 and BC2 coatings as both contain similar fractions of β-NiAl. It is more useful to consider that most MCrAlY alloys comprise β-NiAl and γ-Ni, and so the DBTT of most MCrAlY's is therefore inversely proportional to the phase fraction γ-Ni. This general trend is consistent with the current findings as the BC2 coating exhibits a lower phase fraction of γ-Ni and a higher DBTT compared to the BC1 coating. The BC1 and BC2 coatings (14 and 27 vol.% γ-Ni respectively) also have a higher DBTT than an MCrAlY coating manufactured using similar spray parameters [20] that contained 70 vol.% γ-Ni and 30 vol.% β-NiAl.

The lower phase fraction of γ-Ni in the BC2 coating can be attributed to the addition of 4 wt.% Ta, which promoted the formation of γ'-Ni_3Al: Ta was shown to segregate heavily into the γ'-Ni_3Al by EDX measurements. The formation of γ'-Ni_3Al restricted the amount of Ni available to form γ-Ni, which in turn created a surplus of Co and Cr that led to the formation of σ-Cr_2Co. Therefore, it is possible to state that the addition of 4 wt.% Ta increased the DBTT of coating BC2 due to the subsequent formation of γ'-Ni_3Al and σ-Cr_2Co which lowered the phase fraction of the ductile γ-Ni phase.

5.2 Influence of Microstructure on Fracture Behaviour

In order to understand the change in tensile behaviour of each coating above and below the DBTT, and how this is influenced by the coating microstructures, it is necessary to consider the macroscopic and microscopic fracture behaviour of each coating. The macroscopic fracture patterns of the coatings show distinct characteristics above and below the ductile to brittle transition temperatures (600-700 °C and 650-750 °C for coatings BC1 and BC2 respectively). At 500 °C, below the DBTT of both coatings, cracking occurred in the centre of the tensile surface of the specimens. The cracking was associated with load-drops in the load-displacement curves and for each coating occurred at low strain. As the initial cracks became larger, the central regions of the specimens fractured into multiple fragments. These fragments eventually sheared away from the specimens as the tests continued. This also caused layers of coating to shear away from the tensile surface of the specimens. This additional shearing can be explained by the model shown in Figure 14a: the initial radial cracks propagated to a small distance through the thickness of the specimen, as the central fragments then deformed normal to the specimen under the movement of the punch head, the sub-surface cracks spread through the horizontal plane of the specimen, causing the outer layer to detach. For the BC2 coating, the initial cracks propagated to the edge of the specimen, which is evidence that the magnitude of cracking was higher in the BC2 coating than in the BC1 coating. As the γ-Ni phase is known to be a ductile phase, it can be assumed that during a SPT test it plastically deforms and dissipates energy. Hence, the lower phase fraction of γ-Ni phase in the

BC2 coating resulted in less energy dissipation during bending and a larger release of energy during crack propagation.

The macroscopic fracture patterns of both coatings above the DBTT are characterised by circumferential cracking at a radial offset from the centre of the specimen, as shown in Figure 14b. Experimental observations and finite element models of the SPT test [31-32] have reported this type of failure and it is known to be characteristic of the small punch test for ductile materials. Specimen failure occurs at a circumferential offset because this is the area of maximum principle stress and corresponds to the location of the maximum thinning and plastic strain in the specimen.

The change in macroscopic fracture behaviour below and above the DBTT can be understood by considering the evolution of the stress distribution within a SPT specimen. Finite element models [31-32] have shown that the region of high tensile stress develops underneath the punch contact area. At low displacements the punch contact boundary, and therefore region of high tensile stress, is limited to the centre of the specimen [31]. As the displacement increases the region of high tensile stress shifts radially as the punch contact area increases. The region of high tensile stress then stabilises at a radial offset that corresponds to the radius of the punch head. Below the DBTT of coatings BC1 and BC2, cracking occurs at low strain when the high tensile stress region is in the centre of the specimen. Above the DBTT, cracking occurs at high strain when the high stress region is at a radial offset from the centre of the specimen.

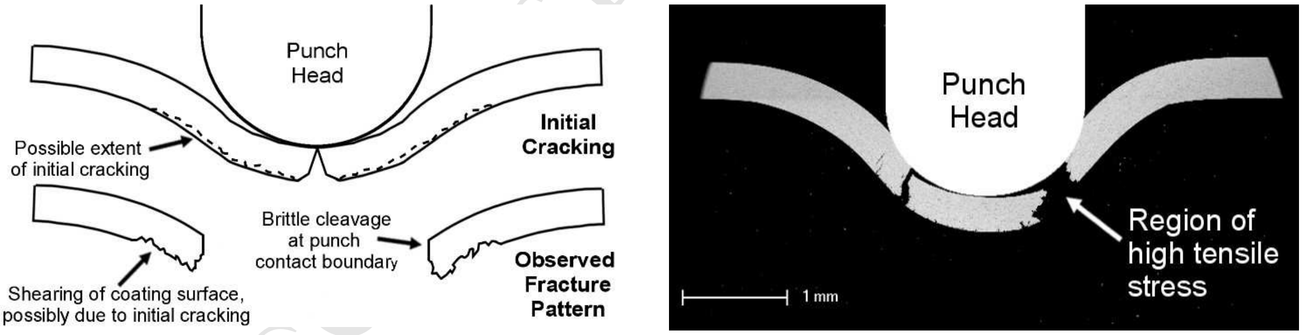

(a) (b)

Figure 14. Schematics showing the macroscopic fracture pattern development of the BC1 and BC2 coatings during SPT tests (a) below and (b) above the DBTT.

Further understanding of the change in tensile and fracture behaviour of coatings BC1 and BC2 can be gained by considering the microscopic fracture behaviour of each coating. The main mode of crack propagation in the BC1 and BC2 coatings was intergranular fracture. This type of fracture is commonly observed in dual-phase (DP) steels, which typically consist of a ductile matrix phase inter-dispersed with hard precipitates. DP steels can be considered similar to the ductile γ-Ni and hard β-NiAl and σ-Cr_2Co phases in the BC1 and BC2 coatings. During plastic deformation of a dual phase steel, yielding starts in the soft ferrite phase whereas the hard martensite phase remains elastic. The strain incompatibility at the phase boundaries causes a build-up of local stress at the phase interface as well as internal stress in the martensite phase [40-42]. Once the internal stress surpasses the elastic limit of the hard phase, it either begins to deform or fractures. The strain incompatibility between the soft and hard phases also causes shearing of the phase interface which leads to void formation [41, 43-44].

Figure 15 shows a simple model of a coating that contains γ-Ni and β-NiAl phases and subject to uni-axial tensile loading, where the γ-Ni and β-NiAl phases are considered to behave in a similar way to the ferrite and martensite phases in dual-phase steels: γ-Ni phase is known to be ductile and does not experience a DBTT [45]; whereas the β-NiAl phase, depending upon composition and processing method, experiences a DBTT between 400-900 °C [1, 39].

Under tensile loading, the γ-Ni phase plastically deforms, which leads to a build-up of local stress at the phase boundaries as well as internal stress in the β-NiAl phase. At low temperature, voids and cracks form at the phase boundaries when the γ-phase deforms but the β-NiAl phase remains inelastic. This causes intergranular fracture as seen in the BC1 and BC2 coatings at 500 °C. At high temperature, the β-NiAl phase becomes ductile and deforms elastically. Voids and/or cracks still develop at the phase boundaries, but a higher amount of plastic deformation and thinning is achieved before intergranular fracture occurs.

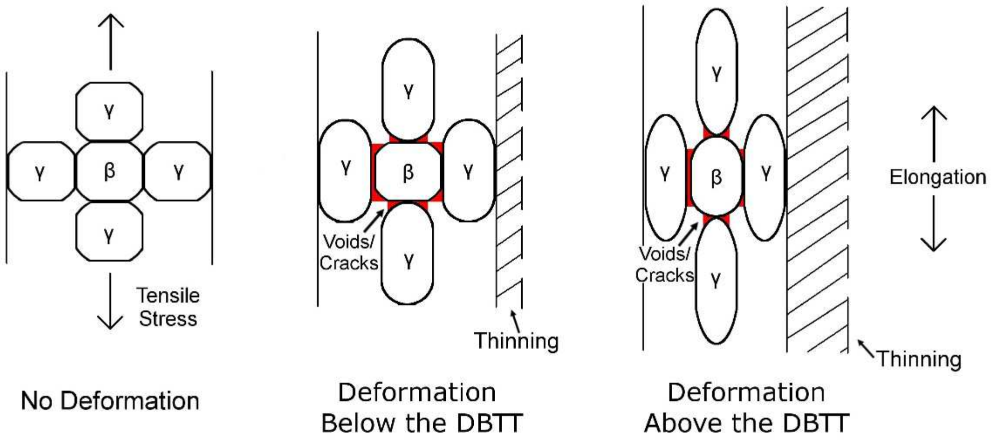

Figure 15. Schematic of void formation for a coating containing γ-Ni and β-NiAl phases subject to tensile loading below and above the DBTT.

Figure 16a shows a similar model for a coating containing γ-Ni, β-NiAl and σ-Cr_2Co. In this instance the σ-Cr_2Co phase can be considered to be a hard undeformable phase that deforms less than the γ-Ni and β-NiAl phases. In this instance, voids and cracks form at the phase boundaries between the three phases, as was observed for both coatings. As intergranular fracture is the dominant fracture mechanism in both coatings, an increase in the number of phase boundaries will increase the density of cracking and decrease the strain to fracture. A reduction in the amount of ductile γ-Ni phase will also reduce the strain to fracture, as was seen for the BC2 coating which contained a higher volume fraction of σ-Cr_2Co phase and lower volume fraction of γ-Ni phase compared to the BC1 coating. The presence of γ'-Ni_3Al phase did not appear to increase the density of crack formation in the BC2 coating, which can be attributed to the coherent interface between the γ-Ni and γ'-Ni_3Al phases [45].

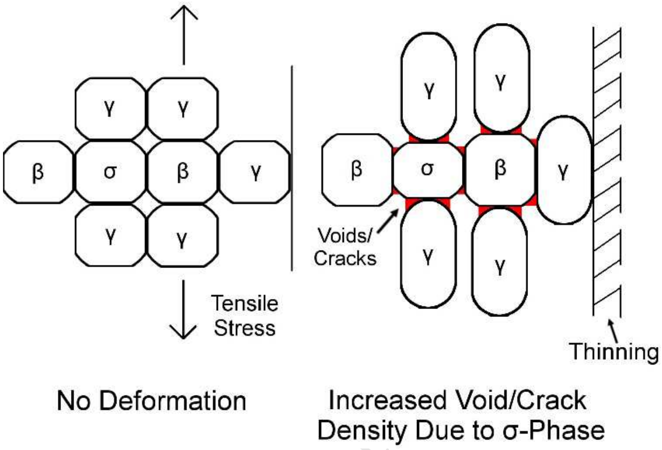

Figure 16. Schematic of void formation for a coating containing γ-Ni, β-NiAl and σ-Cr_2Co phase subject to tensile loading below the DBTT.

5. Conclusions

- The DBTT's of the BC1 and BC2 coatings are 600-700 and 650-750 °C respectively. This is the first time the DBTT’s of these alloys has been determined.
- Decreasing the fraction of γ-Ni phase was shown to increase the DBTT, and reduce the ductility of the HVOF NiCoCrAlY coatings. The presence of σ-Cr_2Co phase also reduced the ductility of the BC2 coating. The presence of γ'-Ni_3Al did not appear to significantly reduce the ductility of the BC2 coating.
- Below the DBTT of coatings BC1 and BC2, fracture occurred at low strain and was characterised by cracking in the centre of the specimen. Above the DBTT, circumferential cracking occurred at a radial offset from the centre of the specimen at high strain.
- Intergranular fracture was the main mode of fracture in the BC1 and BC2 coatings above and below the DBTT’s and is considered to have occurred due to strain incompatibility between the different phases.

Acknowledgements. The authors would like to thank the University of Nottingham for the continued financial support towards this work and would like to acknowledge Shane Maskill for his continued technical support. We would also like to thank Geoff West and Ryan Maclachlan at the University of Loughborough for their assistance in EBSD imaging and the Nanoscale and Microscale Research Centre (NMRC) at the University of Nottingham for their assistance in microscopy.

Data Availability

The raw/processed data required to reproduce these findings cannot be shared at this time as the data also forms part of an ongoing study.

References

[1] S. Bose. High Temperature Coatings. Butterworth-Heinemann, 2007.

[2] A.G. Evans, D.R. Mumm, J.W. Hutchinson, G.H. Meier, and F.S. Pettit. Mechanism controlling the durability of thermal barrier coatings. Progress in Materials Science, 46, 2001.

[3] Y.H. Sohn, J.H. Kim, E.H. Jordan, and M. Gell. Thermal cycling of EB-PVD/MCrAlY thermal barrier coatings: I. microstructural development and spallation mechanisms. Surface and Coatings Technology, 146-147:70–78, 2001.

[4] E. Lugsheider, C. Herbst, and L. Zhao. Parameter studies on high-velocity oxy-fuel spraying of MCrAlY coatings. Surface and Coatings Technology, 108-109:16–23, 1998.

[5] Y. Itoh and M. Saitoh. Mechanical properties of overaluminized MCrAlY coatings at room temperature. Journal of Engineering for Gas Turbines and Power, 127:807–813, 2005.

[6] V. Higuera, F.J. Belzunce, and J. Riba. Influence of the thermal-spray procedure on the properties of a CoNiCrAlY coating. Surface and Coatings Technology, 200:5550–5556, 2006.

[7] B. Gleeson. Corrosion and Environmental Degradation, volume 2 of Materials Science and Technology, chapter High-Temperature Corrosion of Metallic Alloys and Coatings, pages 173{228. Wiley-VCH, 2000.

[8] T. Giampaolo. Gas Turbine Handbook: Principles and Practice. The Fairmont Press, 5th edition, 2013.

[9] D.R.G. Achar, R. Munoz-Arroyo, L. Singheiser, and W.J. Quadakkers. Modelling of phase equilibria in MCrAlY coating systems. Surface and Coatings Technology, 187:272–283, 2004.

[10] J. Toscano, A. Gil, T. Huttel, E. Wessel, D. Naumenko, L. Singheiser, and W.J. Quadakkers. Temperature dependence of phase relationships in different types of MCrAlY - coatings. Surface and Coatings Technology, 202:603–607, 2007.

[11] C. Costa, E. Barbareschi, P. Guarnone, and G. Borzone. Phase evolution in an MCrAlY coating during high temperature exposure. Journal of Mining and Metallurgy, Section B: Metallurgy, 48(3):359–365, 2012.

[12] M. Eskner and R. Sandstrom. Mechanical properties and temperature dependence of an air plasma-sprayed NiCoCrAlY bondcoat. Surface and Coatings Technology, 200(8):2695 – 2703, 2006.

[13] A.K. Ray, N. Roy, A. Kar, A.K. Ray, S.C. Bose, G. Das, J. K. Sahu, D. K. Das, B. Venkataraman, and S. V. Joshi. Mechanical property and characterization of a NiCoCrAlY type metallic bond coat used in turbine blade. Materials Science and Engineering: A, 505(12):96 – 104, 2009.

[14] S. Saeidi, Voisey K.T., and D.G. McCartney. Mechanical properties and microstructure of VPS and HVOF CoNiCrAlY coatings. Thermal Spray Technology, 20(6):1231–1243, 2011.

[15] H.Y. Qi, L.Z. Zhou, and X.G. Yang. Measurement of Young’s modulus and Poisson’s ratio of thermal barrier coatings. Chinese Journal of Aeronautics, 18(2):180–184, 2005.

[16] T.A. Taylor and D.F. Bettridge. Development of alloyed and dispersion-strengthened MCrAlY coatings. Surface and Coatings Technology, 86-87:9–14, 1996.

[17] A.K. Ray. Failure mode of thermal barrier coatings for gas turbine vanes under bending. International journal of turbo and jet-engines, 17(1):1–24, 2000.

[18] K.J. Hemker, B.G. Mendis, and C. Eberl. Characterizing the microstructure and mechanical behaviour of a two-phase NiCoCrAlY bond coat for thermal barrier systems. Materials Science and Engineering A, 483-484:77–730, 2008.

[19] H. Chen, T.H. Hyde, Voisey K.T., and D.G. McCartney. Application of small punch creep testing to a thermally sprayed CoNiCrAlY bond coat. Materials Science and Engineering: A, 585:205–213, 2013.

[20] G.A. Jackson, W. Sun, D.G. McCartney. The Application of the Small Punch Tensile Test to Evaluate the Ductile to Brittle Transition of a Thermally Sprayed CoNiCrAlY Coating, Key Engineering Materials, Vol. 734, pp. 144-155, 2017

[21] F.M. Huang and M.L. Hamilton. Bend testing for miniature disks. Nuclear Technology, 57(2):234–242, 1982.

[22] J. Kameda and X. Mao. Small-punch and TEM-disc testing technique and their application to characterization of radiation damage. Journal of Materials Science, 27(4):983–989, 1992.

[23] X. Mao. Small punch test to predict ductile fracture toughness JIC and brittle fracture toughness KIC. Scripta Metallurgica et Materialia, 25:2481–2485, 1991.

[24] H. Li, F.C. Chen, and A.J. Ardell. A simple versatile disk-bend test apparatus for quantitative yield-stress measurements. Metallurgical and Materials Transactions A: Physical Metallurgy and Materials Science, 22(9):2061–2068, 1991.

[25] A. Okada and M. Hamilton. Microbulge testing applied to neutron irradiated materials. Journal of Nuclear Materials, 179:445–448, 1991.

[26] V. Vorlicek, L.F. Exworthy, and P.E.J. Flewitt. Evaluation of a miniaturized disc test for establishing the mechanical properties of low-alloy ferritic steels. Journal of Materials Science, 30(11):2936–2943, 1995.

[27] E. Altstadt, H.E. Ge, V. Kuksenko, M. Serrano, M. Houska, M. Lasan, M. Bruchhausen, J.M. Lapetite, and Y. Dai. Critical evaluation of the small punch test as a screening procedure for mechanical properties. Journal of Nuclear Materials, 472:186–195, 2016.

[28] S. Saeidi, Voisey K.T., and D.G. McCartney. The effect of heat treatment and the oxidation behaviour of HVOF and VPS CoNiCrAlY coatings. Journal of Thermal Spray Technology 18. 209–216, 2009.

[29] CEN CWA 15627 Worskshop Agreement: Small punch test method for metallic materials. European Committee for Standardization, Brussels, December 2006.

[30] X. Mao, T. Shoji, and H. Takahashi. Characterization of fracture behaviour in small punch test by combined recrystallization-etch method and rigid plastic analysis. Journal of Testing and Evaluation, 15(1): 30-37, 1987.

[31] R.J. Lancaster, H.W. Illsley, G.R. Davies, S.P. Jeffs, and G.J. Baxter. Modelling the small punch tensile behaviour of an aerospace alloy. Materials Science and Technology, Vol 33 (9) 2017.

[32] M. Abendroth and M. Kuna. Identication of ductile damage and fracture parameters from the small punch test using neural network. Engineering Fracture Mechanics. Vol 73. 710-725, 2006.

[33] R. Hurst and K. Matocha. Experiences with the european code of practice for small punch testing for creep, tensile and fracture behaviour. In Determination of Mechanical Properties of Materials by Small Punch and Other Miniature Testing Techniques, pages 1-26, September 2014.

[34] C. Duret-Thual, R. Morbioli, and P. Steinmetz. A guide to the control of high temperature corrosion and protection of gas turbine materials. Technical report, Commission of European Communities, 1986.

[35] M. Eskner and R. Sandstrom. Measurement of the ductile-to-brittle transition temperature in a nickel aluminide coating by a miniaturised disc bending test technique. Surface and Coatings Technology, 165(1):71 – 80, 2003.

[36] S. Rasche and M. Kuna. Improved small punch testing and parameter identification of ductile to brittle materials. International Journal of Pressure Vessels and Piping, 125: 23-34, 2015.

[37] R. Lacalle, J.A. Alvarez, and F. Gutierrez-Solana. Analysis of key factors for the interpretation of small punch test results. Fatigue and Fracture of Engineering Materials and Structures, 31(10):841–928, 2008.

[38] M.G. Hesbur and R.V. Miner. High temperature tensile and creep behaviour of low pressure plasma-sprayed NiCoCrAlY coating alloy. Materials Science and Engineering, 83:239-245, 1986.

[39] D.B. Miracle and R. Darolia. Structural Applications of Intermetallic Compounds. Chapter: NiAl and It's alloys. 55-74. John Wiley and Sons, 2000.

[40] M. Calcagnotto, Y. Adachi, D. Ponge, and D. Raabe. Deformation and fracture mechanisms in fine- and ultrafine-grained ferrite/martensite dual-phase steels and the effect of aging. Acta Materialia, 59:658-670, 2011.

[41] J. Kadkhodapour, A. Butz, and S. Ziaei Rad. Mechanisms of void formation during tensile testing in a commercial, dual-phase steel. Acta Materialia, 59(7): 2575-2588, 2011.

[42] K. Park, M. Nishiyama, N. Nakada, T. Tsuchiyama, and S. Takaki. Effect of the martensite distribution on the strain hardening and ductile fracture behaviours in dual-phase steel. Materials Science and Engineering: A, 604:135-141, 2014.

[43] C.C. Tasan, J.P.M. Hoefnagels, and M.G.D. Geers. Microstructural banding effects clarified through micrographic digital image correlation. Scripta Materialia, 62 (11):835-838, 2010.

[44] H.P. Shen, T.C. Lei, and J.Z. Liu. Microscopic deformation behaviour of martensitic-ferritic dual-phase steels. Materials Science and Technology, 2(1): 28-33, 1986.

[45] R.C. Reed. Superalloys - Fundamentals and Applications. Cambridge University Press, 2006.